6-13-2022

Bathymetry Based Modeling of Subaxial Magma Flows Under the Mid-Atlantic Ridge, 0 to 30° N

Adam R. Tjoelker
Calvin University, adamtjoelker@gmail.com

Neil Van Kanegan
Calvin University, neilvankanegan@gmail.com

Simon Detmer
Calvin University, sendetmer@gmail.com

C. Renee Sparks
Hope College, sparks@hope.edu

Follow this and additional works at: https://digitalcommons.csbsju.edu/compass

Part of the Tectonics and Structure Commons

Recommended Citation

Bathymetry Based Modeling of Subaxial Magma Flows Under the Mid-Atlantic Ridge, 0 to 30° N

Adam R. Tjoelker[1], Neil Van Kanegan[1], Simon Detmer[1], and C. Renee Sparks[2]

[1]Department of Geology, Geography, and Environment
Calvin University
3201 Burton St SE
Grand Rapids, MI 49546 USA
adamtjoelker@gmail.com
neilvankanegan@gmail.com
sendetmer@gmail.com

[2]Geological and Environmental Sciences Department
Hope College
141 E 12th St
Holland, MI 49423 USA
sparks@hope.edu

ABSTRACT

Fracture patterns of the Mid-Atlantic Ridge (MAR) provide evidence of tectonic forces related to divergence and magma upwelling at the ridge axis. In this study, we focus on the MAR from 0 to 30° N, where the N-S ridge exhibits slow spreading rates (2-4 cm/yr) and pronounced axial topography. Ridge segments and transform faults identified in bathymetry data were analyzed for strike orientation and axial depth profiles. Azimuths of transform faults and ridge segments exhibit increasing clockwise rotation with latitude, and all have left lateral displacement. Bathymetric sampling along ridge segments occurred at 9 km intervals with 20 km sampling radii, producing axial lithostatic pressure gradients. One-dimensional magma flows parallel to the ridge axis at 10 and 50 km depths were modeled using Darcy's law based on published parameters and calculated gradients. Subaxial magma velocities of up to 4 cm/yr were predicted for horizontal flow at depth and are comparable in magnitude to upwelling rates in published literature. Average flow magnitudes (n = 422) within the melt generation region are predicted at 0.8 and 0.2 cm/yr for 10 and 50 km depths respectively. Flow velocities up to five times higher are expected with this model in the high-porosity boundary layer below the solidus. The Coriolis parameter

would affect the movement of the flows predicted by our model and may be linked to rotational patterns observed at the MAR. Future research of magma migration below divergent margins would benefit from incorporating axial lithostatic load variations as a driver of flow.

KEY WORDS: Mid-Atlantic Ridge, Magma Flow, Tectonic Fabric, Lithostatic Pressure, Bathymetry, Mid-Ocean Ridge, Divergent Margins

INTRODUCTION

The study area for the current investigation includes the Mid-Atlantic Ridge (MAR) system from the Equator to 30° north latitude. In its entirety, the MAR system runs from around 87° N to 54° S through roughly the center of the Atlantic Ocean. The width of the Ridge ranges from 1000-1300 km (Liu et al., 2021). After conducting a similar study of the MAR system from the Equator to 30° S latitude, (Detmer et al., 2021 in review), the addition of magmatic modelling in this study enables continued investigation of the MAR's tectonic fabric and allows us to test our hypotheses for the driving factors of ridge morphology.

The purpose of this study is to examine and explain the observed tectonic processes, magmatic flow and morphology of the ridge system in light of lithostatic pressure induced subaxial magma flows along the ridge axis. These subaxial magma flows may be responsible for patterns identified in the fracturing and divergence of the MAR within the study area. Our research involves the use of ocean floor bathymetry data provided by the General Bathymetric Chart of the Oceans (GEBCO), to enable the analysis of the regional tectonic fabric of the MAR and develop our subaxial magma flow models from bathymetry based lithostatic pressure modeling.
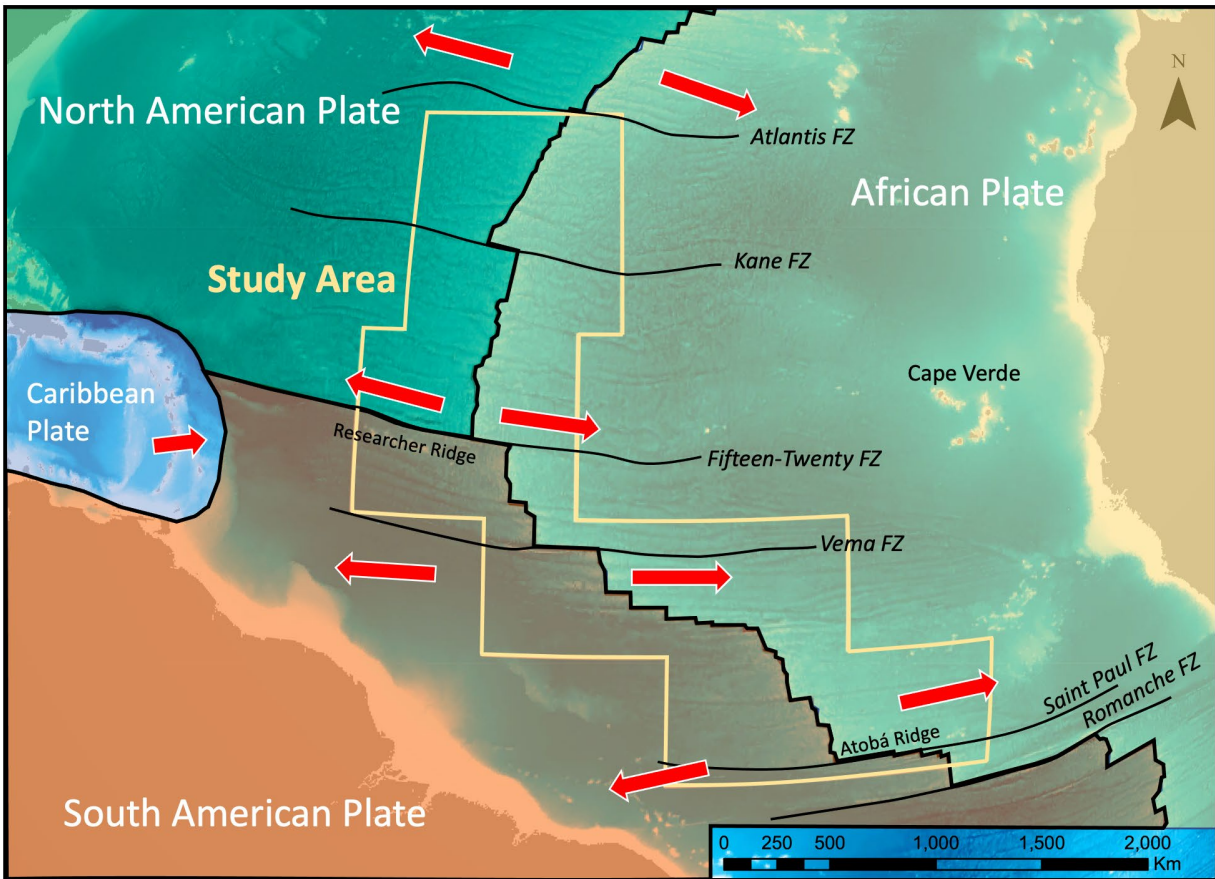
Figure 1. Overview of the MAR study area and surrounding features. Several, but not all, of the fracture zones (FZ) are shown for geographic context. Red arrows provide relative motion between tectonic plates.

BACKGROUND

Mid-Atlantic Ridge System Features

Features of the ocean floor found along or near the ridge system are evident within the GEBCO bathymetry data. Bathymetry for this region is variable in spatial resolution, with much of the MAR system mapped with high resolution multi-beam sonar data.

In areas where sonar imaging has not been conducted or is not publicly available, GEBCO provides depths which are mathematically modeled and interpolated using sea-surface elevation differences measured by satellite radar altimetry from the base Version 2 of the SRTM15+ global dataset (Tozer et al., 2019).

Our study area represents a part of the MAR that contains a wide diversity of morphological characteristics (Fig. 1). According to Moores and Twiss (2014), a mid-ocean ridge can be described as a topographic swell on the ocean floor relative to the abyssal plains of the ocean basin on either side. Ridge segment morphology can be correlated to spreading rates with reference to the type of relief exhibited (Brown and White, 1994; Carbotte and Macdonald, 1994).

The MAR exhibits slow spreading rates (Macdonald and Fox, 1990; Macdonald et al., 1991; Mallows and Searle, 2012; Liu et al., 2021) of approximately 2-4 cm/yr. Spreading rates in our study area (the northern part of the MAR) are slower than rates in the southern part (Liu et al., 2021). Selected studies also predict long-term spreading asymmetry in terms of differing accretionary rates on either side of the ridge axis (Mallows and Searle, 2012). Researchers have hypothesized that at slow-spreading ridges such as the MAR, oceanic crust is built through magmatic accretion, (Mallows and Searle, 2012) and the aggregation of volcanoes fueled by temporary magma chambers (Briais et al., 2000). The crustal spreading rate is also correlated with magmatic supply and activity at the MAR. Higher spreading rates are associated with higher magma supply, which in turn causes magmatic activity and features to be more prevalent. Slower spreading rates are associated with a lower amount of magma, and thus a lower amount of magmatic activity and features (Liu et al., 2021).

Transform or shear-related ridges are also prevalent in the vicinity of the MAR, (Macdonald et al., 1991) as shown in Figure 1. These include the Atobá Ridge, (running E-W) (Marcia et al., 2016; Mohriak, 2020) which includes the Saint Peter and Saint Paul Archipelago associated with recent regional uplift (Motoki et al., 2014). Of particular interest is Researcher Ridge, found slightly west of the MAR, at around 15° N. Researcher Ridge is a volcanic chain, oriented WNW-ESE, (orthogonal to the axis of the MAR) and is composed of a series of around seven seamounts, including two guyots. Upwelling that resulted from the vertical migration of a plume associated with a hotspot is hypothesized to have produced this chain of seamounts (Long et al., 2019).

Deep fracture zones are well attested in the geologic literature as aligning with transform offsets of MAR segments in the study area of 0 to 30° N. Fracture zones demonstrating this phenomenon include the Atlantis Fracture Zone, (Canales et al., 2004) (running from approximately 29° N, 37° W to 30°45' N, 45°30' W) the Kane Fracture Zone, (Cormier et al., 1984; Auzende et al., 1994) (running from approximately 22°40' N, 40° W to 24°30' N, 50° W) and the Fifteen-Twenty Fracture Zone, (Roest and Collette, 1986) (running from approximately 14° N, 36°30' W to 15°30' N, 47°30' W).

Other topographic highs just outside of the study area provide context for the tectonic forces at work. The Atlantis Megamullion rises well above the MAR rift valley at approximately 30° N exhibiting structural displacement and volcanic vent activity (Canales et al., 2004). To the east of the study area, the islands composing Cape Verde mark a topographic high possibly associated with a structural dome. Basins such as the Gambia Basin (Spathopoulos and Jones, 1993) or smaller deep fracture zones are often found accompanying these areas of high tectonic relief.

Tectonics in the MAR System

The North and South American tectonic plates consist of oceanic lithosphere along the MAR as well as thicker continental lithosphere to the west. For this study, we focus on the interaction between these plates and the African Plate to produce the MAR and associated features through divergence. Active tectonic divergence is evident through earthquake activity along ridge and transform sections of the MAR system. To the north and east of the study area, relative movement of the North American Plate continues to produce divergence which increases in complexity as the plate emerges from a triple junction with the Eurasian and African plates. Continuing southward within the study area, the plate divergence between the South American Plate and the African Plate occurs. In this area, seismic activity is abundant along ridge and transform segments of the MAR as tensional stresses act on the boundary between these two plates. Similar to the North American Plate, the South American Plate consists of oceanic lithosphere to

the east and continental lithosphere to the west. The Andes Mountains along the western margin of the South American Plate represent the most extensive continental volcanic arc currently forming on Earth. This continental volcanic arc boundary is evidence of convergence suggesting that the South American Plate is moving westward. Therefore, the relative motion between the South American and African plates at the MAR is divergent, and this motion continues well into the Southern Hemisphere. As is similar between the North American and African plates, oceanic crust is produced at the MAR and provides evidence of this critical component of tectonic activity.

However, these divergent tectonic margins are not the only plate interactions affecting the region. The North American Plate also interacts with the Caribbean plate to produce a convergent plate boundary, complete with the Puerto-Rican trench and the Lesser Antilles volcanic arc. At this tectonic boundary, the North American Plate is subducting to the west, beneath the Caribbean plate. This motion is accompanied by seismic activity along the Waditi-Benioff zone, which extends under the Caribbean plate. Volcanic activity which produces islands within the Lesser Antilles volcanic arc also provides evidence of magma generation through flux melting at depth.

Not all plate boundaries in the study area are actively moving with respect to each other. The boundary between the North American Plate and the South American Plate is seismically inactive in comparison to other boundaries. Using fault geometry and orientation analyses of deformation, the boundary between these two plates has been inferred as being located around 16° N (Roest and Collette, 1986).

The relative motion and rate of tectonic divergence provides an overall picture of plate movement that contributes to global tectonics. However, one of the most complex aspects of global-scale tectonic studies is determining the reference point for relative motion. For example, if the position of the stable crustal material of the African Plate is our spatial reference, this study would conclude that the North American and South American plates are pulling away toward the west at rates between 2-4

cm/yr (Brown and White, 1994; Carbotte and Macdonald, 1994). Though the relationship between the North American and Caribbean plates ranges from convergent to transform, studies suggest general westward motion of both plates (Moores and Twiss, 2014). Comparatively, if our reference is the North American Plate, then the African, Eurasian, and Caribbean plates would all appear to have an eastward motion. As a result, this study will reference relative motions between major plates and discuss forces acting at those boundaries to estimate motion vectors with components of rate and direction. These vector components can lead to decompression which generates magma at the MAR and can also manifest as fault movements and seismic activity.

Since oceanic crust is produced as a result of volcanic and plutonic activity at the MAR boundary, it preserves the history of tectonic divergence as recorded in magnetic reversals. In general, these magmatic histories are preserved in a mirrored pattern of normal and reversed magnetic polarity and can be used to determine relationships between spreading rates and oceanic crustal thicknesses (Brown and White, 1994). The distance and spacing of magnetic reversals have provided spreading rates along the MAR ranging from 2-4 cm/yr (Carbotte and Macdonald, 1994). Though recorded in the minerals of volcanic and plutonic rocks, the pattern of magnetic reversals is not perfectly symmetrical. This results in magnetic anomalies associated with the growth of oceanic crust at mid-ocean ridges. Magnetic anomalies and asymmetry in magnetism across mid-ocean ridge axes are frequently observed phenomena (Khutorskoi and Teveleva, 2019) that suggest differential spreading character.

Magma Genesis and Movement in Mid-Ocean Ridge Systems

In addition to analysis of ocean features and ocean floor tectonics, recent research has focused on modeling magma genesis and migration under mid-ocean ridge systems. The following paragraphs will provide a brief overview of magma generation and examine current hypotheses for magma movement.

The most widely accepted model of magma generation in mid-ocean

ridge systems is decompression melting, which results when heated mantle material migrates toward areas of lower pressure along the axis of divergence as lithospheric plates spread. Decompression lowers the melting point of these heated rocks, causing partial melting (Plank and Langmuir, 1992). Decompression melting typically occurs at temperatures ranging from 1280-1320°C and extends from the base of the oceanic crust to a depth of around 60 km in the upper mantle (Katz, 2008).

Melting of mantle rock and the generation of mafic magma may also be achieved through the addition of volatiles. This results in flux melting, where the melting curve is chemically reduced. Hydration of previously anhydrous silicates can lead to the formation of thicker crust and produce higher melt volumes (Asimow and Langmuir, 2003; Dasgupta and Hirschmann, 2010; Kelley, 2014). Here, the presence of water or carbon dioxide contained within the mineral structures is released during metamorphism. This produces a flux reaction where the liquidus curve is lowered in the phase diagram, and melt

begins. Mineral and compositional signatures testify to the chemical conditions for melt formation, (Asimow and Langmuir, 2003) including the presence of volatiles. A key factor in the composition of a magma is the composition of the oceanic crust itself (Kelley, 2014). Oceanic crustal composition is influenced by the mixing of mantle peridotite melts. Other magma composition-fixing factors include upper mantle viscosity and pressure, as well as ratios between the residual solid and a given melt (Plank and Langmuir, 1992).

During magma genesis, thermodynamics and fluid mechanics play a major role in the motion of magma focusing and the production of oceanic crust. Buoyancy and magmatic focusing are currently thought to be the two main forces that influence magma flow beneath mid-ocean ridge systems. Buoyant rising is explained by the density difference between magma and the residual solid, eventually giving rise to topographic features in a mid-ocean ridge system (Lin and Parmentier, 1989). Periodic temperature fluctuations within the mantle are interpreted as a key factor in the process of buoyant rising that lead to

divergence, continued decompression, and ridge push (Kelley, 2014). According to the enthalpy method, as magma rises toward the mid-ocean ridge axis, the temperature of the melt decreases and melting, porosity, and rising velocity increase. When these values fluctuate between minima and maxima around a given mean, buoyant rising can occur (Katz, 2008).

Buoyant rising appears to be the primary control on melt movement under mid-ocean ridge systems, but horizontal focusing flow is also expected to play a role. At mid-ocean ridge systems where spreading rates are similar to the MAR, crustal thickness is estimated to be around 7 km (Brown and White, 1994). Given this average thickness, if magma merely traveled vertically beneath ridge systems, we would expect to see a smaller value for crustal thickness. Since this isn't observed however, some degree of horizontal transport can be modeled (Sparks and Parmentier, 1991). This horizontal transport is hypothesized to contribute to magma focusing particularly along the solidus boundary of the upper flanks of the melt prism.

This study examines additional factors that could contribute to horizontal flow or magma migration in the area of the MAR system. Components of horizontal flow have the potential to exert additional shear, compressive, or tensional stresses as manifested in rheological responses within the upper lithosphere.

METHODS
Bathymetry Data

The GEBCO 2020 Grid is the primary dataset used for this study. Bathymetry included in this analysis encompasses the MAR from 0 to 30° N. For this range of the MAR, the majority of the ridge is mapped in high detail multi-beam sonar with 15 arc second resolution (which is approximately 450 m). The largest notable gap in high resolution coverage of the ridge axis exists from 7 to 10° N, where there are only low-resolution bathymetry products interpolated from satellite altimetry. The data sources for the GEBCO 2020 ridge bathymetry are shown in Figure 2.
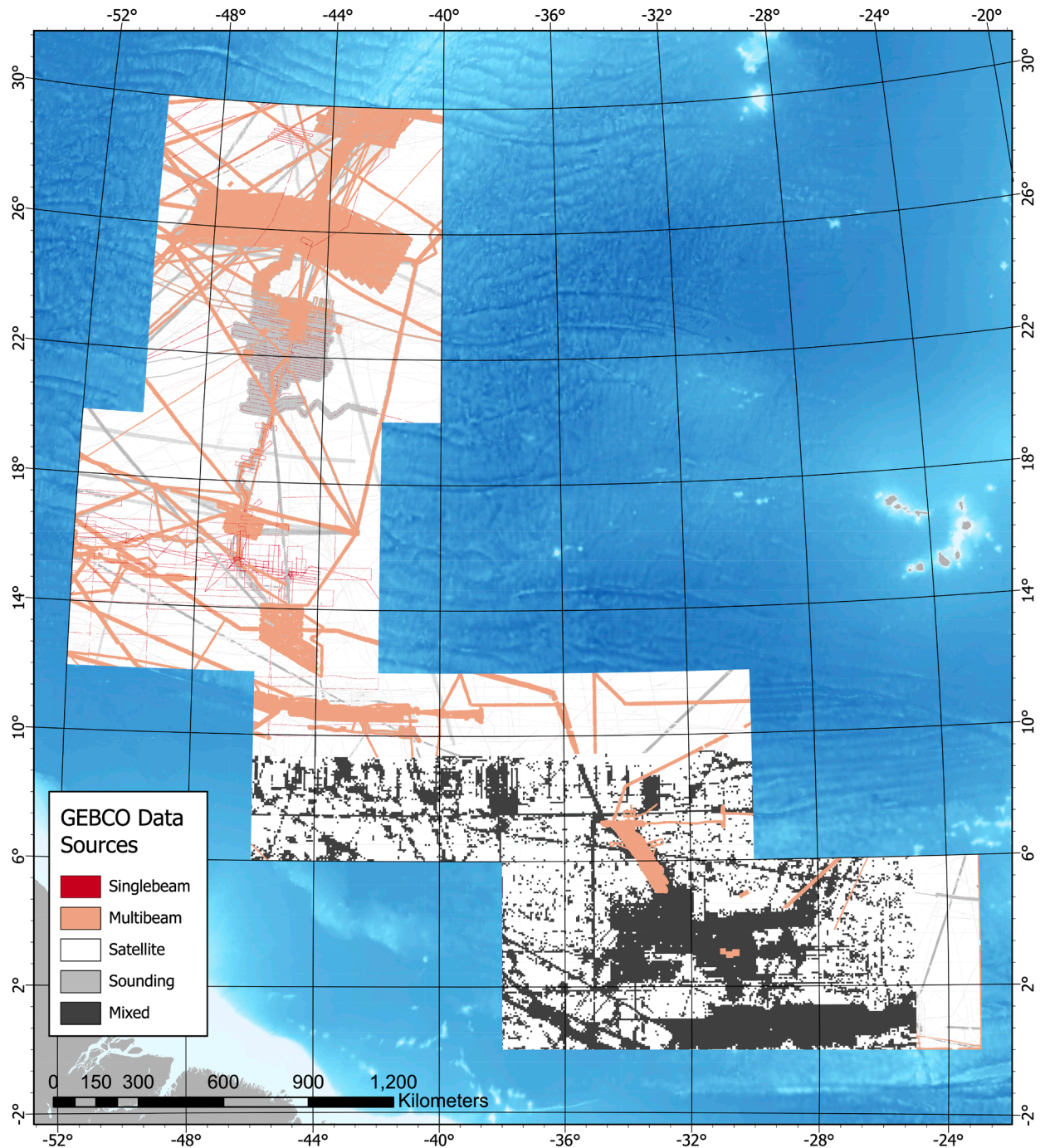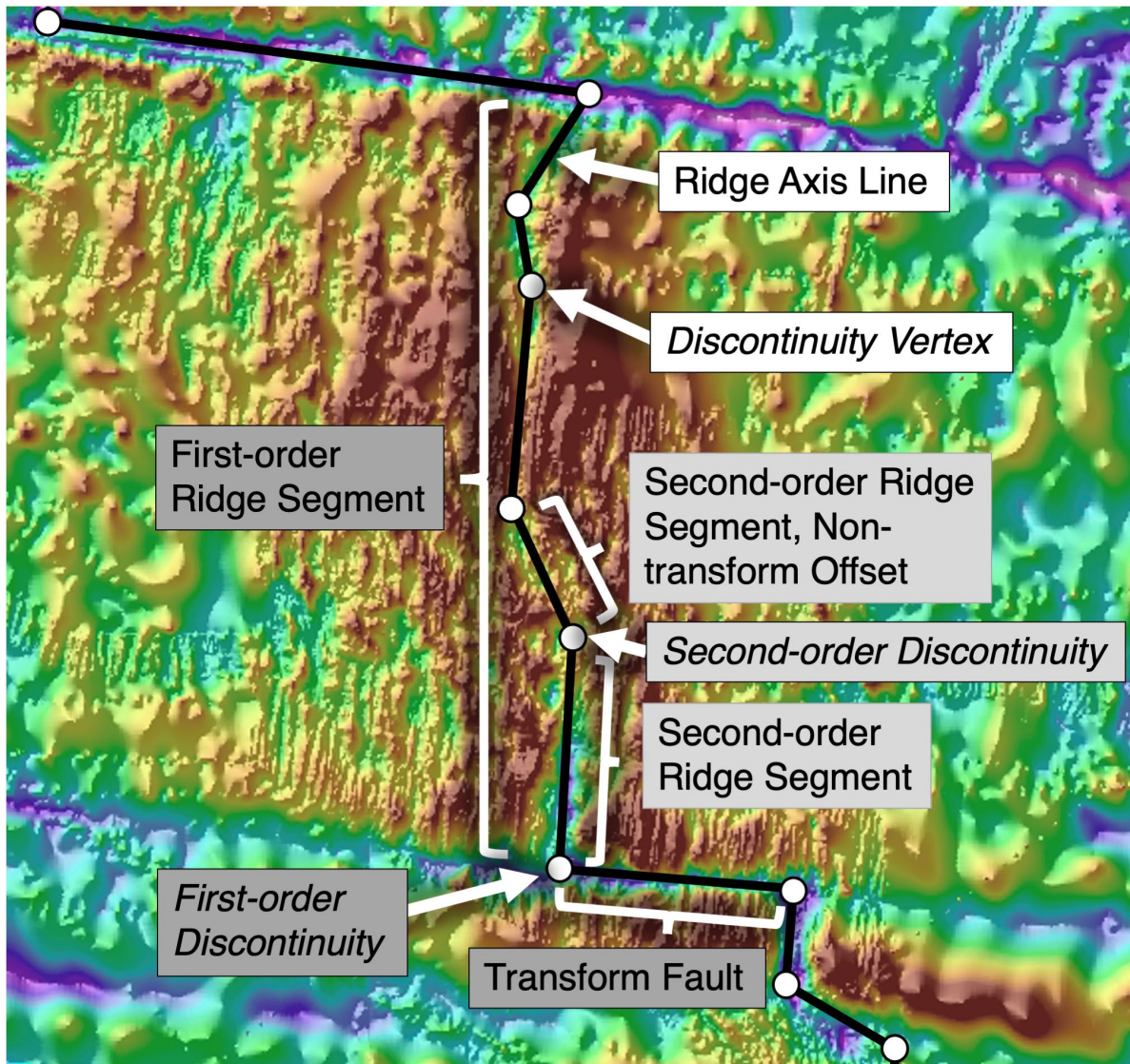
Figure 2. Detailed map of the study area showing the types and location of various bathymetric data sources from the GEBCO_20 Type Identifier (TID) Grid.
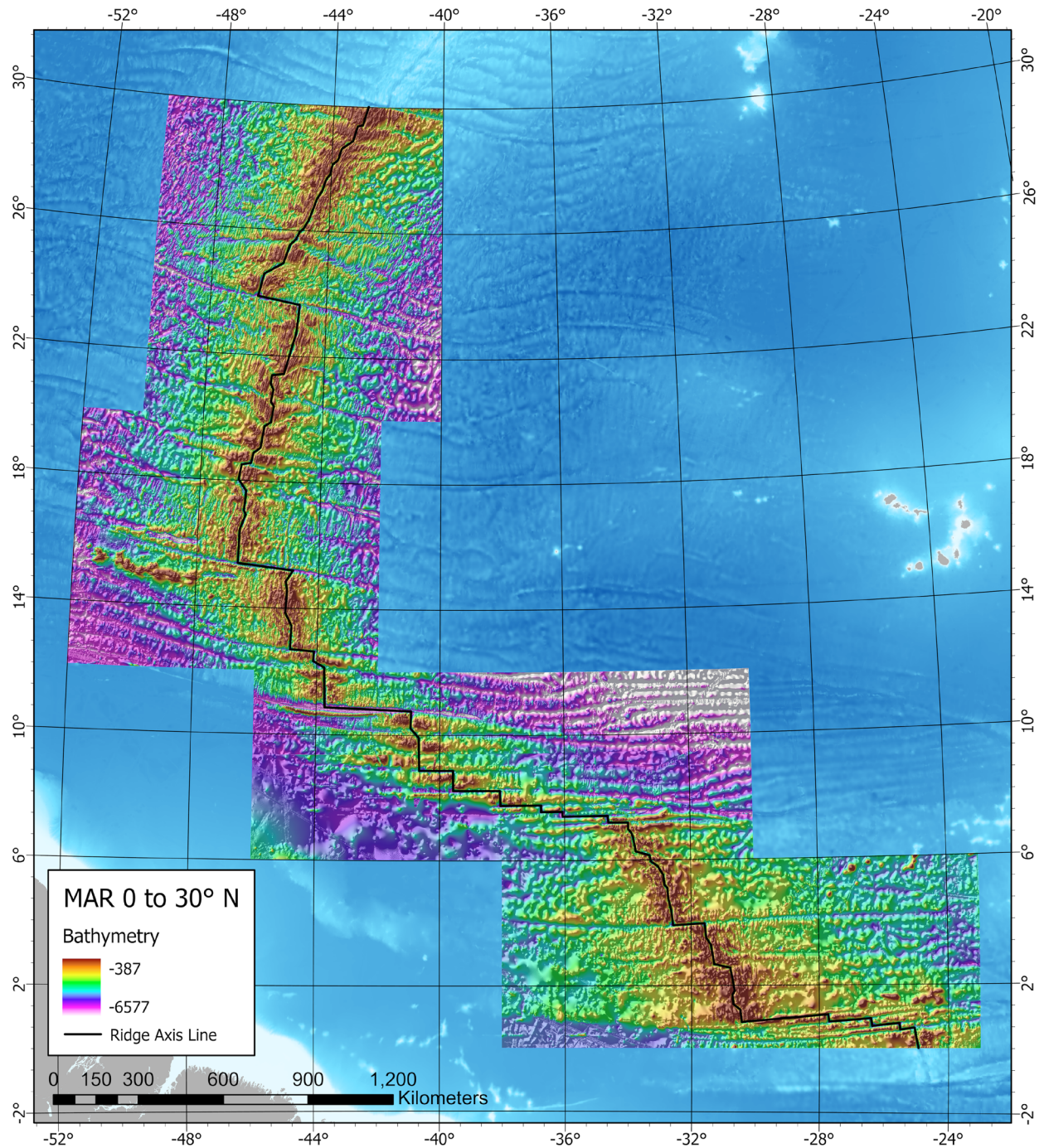
Figure 3. Map of the final processed GEBCO bathymetry for the study area in meters below sea level. A hillshade and sequential color ramp are applied to the data to indicate topography.

Figure 4. A close-up view of the ridge axis line, showing ridge segments, transform faults, discontinuities, offsets, and vertices.

Tectonic Fabric Analysis

For the analysis of the regional tectonic fabric of the MAR, the axis of divergence of the ridge is mapped using GEBCO 2020 Grid bathymetry data. A hillshade and sequential color ramp applied to the raster data enable visual distinction of ridge segments and rift valleys. A map of the processed bathymetry data for the entire study area can be seen in Figure 3. Using GIS software, a ridge axis line drawn down the center of the MAR is used to indicate the location of the slow

spreading rift valley. The direction and placement of the ridge axis line conforms to the axis of divergence of all ridge segments, which is equivalent to the strike azimuth of the ridge segments. Similarly, a single line drawn across the center of each transform fault is added to indicate the fault strike azimuth. Vertices in the ridge axis line exist at the junctions between ridge segments and transform segments at the boundary between first and second-order discontinuities in the ridge system as defined by Macdonald and others, (1991). First-order discontinuities are identified as orthogonal transform offsets in the ridge, dividing the MAR into major first-order ridge segments. Second-order discontinuities split the larger first order ridge segments into second-order ridge segments where the axial valley bends but does not form a transform fault. Diagonal second order ridge segments that do not form a transform fault are called non-

transform offsets. An example of the ridge axis line can be seen in Figure 4. In areas of lower resolution bathymetry, the ridge segments and offsets are approximated across the general features shown in the satellite bathymetry. The result of this process is a continuous line from 0 to 30° N along the axial valley of the MAR which bends to conform to both the azimuth of ridge segments and the strike azimuth of transform offsets between ridge segments. In this analysis, the smallest second order segments likely represent the areas of continuous magmatic focusing and subaxial magma reservoirs along ridge segments (Macdonald et al., 1991).

The coordinates of each discontinuity junction in the ridge axis line are classified as either part of a ridge segment or transform fault. The azimuths along each ridge segment between each point were calculated using a spherical approximation of the Earth:

$$\theta = atan2(\sin(\Delta\lambda)\cos(\phi_2), \cos(\phi_1)\sin(\phi_2) - \sin(\phi_1)\cos(\phi_2)\cos(\Delta\lambda)) \qquad (1)$$

where θ is the angle of bearing between the two points, $\Delta\lambda$ is the difference in longitude, ϕ_1 is the latitude of the first

point, and ϕ_2 is the latitude of the second point. Over the range of latitudes within our study area,

azimuths calculated using the spherical approximation resulted in errors no greater than 0.2° when compared to the high precision calculations using the Geoscience Australia Vincenty Geodetic Calculator. Therefore, the application of this simple spherical geometry azimuth formula results in a negligible error due to the larger error associated with line drawing method. This error potentially varies by a few degrees depending on the placement of the lines approximating the ridge axis. Despite the small variations in the line azimuths, identification of ridge segments was repeatable over multiple applications of our axis line drawing method.

The calculation of azimuths for the ridge segments enables the orientations of the fault and ridge segment azimuths over the entire study area to be visualized. Additionally, the regional morphological trends in the bathymetry data can be investigated using the azimuth data generated for this dataset.

Depth Analysis

In addition to the vertices placed along the discontinuities of each ridge segment, nodes are added at equidistant intervals between each vertex of approximately 9 km along the ridge axis line. At each of these additional nodes and the original ridge axis line vertices, mean bathymetric depth data was gathered from within a sampling buffer of 20 km surrounding each point.

Each depth sample buffer is used to generate the average lithostatic loads at 10 and 50 km depths from the surface of the ocean. Load calculations are a function of the local bathymetry within the 20 km buffer, the theoretical normal gravity term, and the thickness and density assumptions made about the composition of the crust and upper mantle along the MAR.

Overlap exists between the 20 km sampling buffers due to the 9 km separation of additional equidistant sampling nodes along the ridge axis line. This sampling method intends to capture the average load along the ridge and ensure the pressure data is smooth and better represents lithostatic pressures at depth. This also ensures that the errors associated with the satellite bathymetry are minimized due to the larger area of bathymetric sampling for each buffer zone.

Load Analysis

Lithostatic pressure is calculated using a simple pressure formula assuming constant gravitational acceleration in the depths calculated. This model accounts for differing layer densities and thicknesses for the ocean, crust, and mantle under each bathymetry sample buffer. These two depths illustrate the pressure exerted on magma near the top of the mantle at 10 km beneath the crustal surface, where melt begins to cease and magma is focused near the center of the ridge axis, and 50 km beneath the crust, where melting and focusing has begun. The pressure equations used are:

$$P_{10} = g(\phi)\rho_w h_w + g(\phi)\rho_c(h_c - h_s) \tag{2}$$
$$P_{50} = g(\phi)\rho_w h_w + g(\phi)\rho_c(h_c - h_s) + g(\phi)\rho_m(h_m - h_c) \tag{3}$$

where P_{10} and P_{50} are the pressures at 10 and 50 km depths respectively, h_w is the average bathymetric depth below sea level for the buffer zone, h_c is the depth from the ocean surface to the bottom of the oceanic crust (10 km), h_m is a chosen depth from the ocean surface to within the mantle (50 km), $g(\phi)$ is the normal gravity term, or acceleration due to gravity at the surface of the Earth measured at a specific latitude, and ρ_w, ρ_c, and ρ_m are the densities of seawater, (1030 kg/m³) mafic crust, (2900 kg/m³) (Niu and Batiza, 1991) and mantle peridotite (3300 kg/m³) (Simon et al., 2008).

Each normal gravity term was measured at the center of each sample buffer and is defined according to the Somigliana normal gravity equation, which is derived from the WGS 84 ellipsoid as:

$$g(\phi) = g_e \frac{1 + k\,sin^2(\phi)}{\sqrt{1 - e^2\,sin^2(\phi)}} \tag{4}$$

where g_e is the normal gravity at the equator (9.780325336 m/s²), k is a dimensionless constant accounting for the semi-major and semi-minor axes of the ellipsoid and the normal gravity at the equator and poles (1.913185×10^{-3}), e^2 is the first eccentricity of the ellipsoid squared (6.69438×10^{-3}), and ϕ is the latitude of the center of the buffer. All constants for this equation

are defined in the National Geospatial-Intelligence Agency Standardization Document (2014).

Magma Flow Analysis

Magma flow is modeled using the one-dimensional form of Darcy's law for flow approximated as an incompressible fluid in an isotropic porous medium. The flow direction modeled is parallel to the axis of divergence along second-order ridge segments from 0 to 30° N. Magma flow is not modeled along transform faults since significant melt concentration is primarily directed towards ridge segments in the vicinity of transform offsets (Weatherley and Katz, 2010). Solving for the flow velocity, Darcy's law (5) was rearranged to incorporate the dependence of the permeability on porosity (6) from Sparks and Parmentier (1991), with the final form derived for this model given in (7):

$$u = \frac{k}{\mu L \phi} \Delta p \qquad (5)$$
$$k = k_0 \phi^3 \qquad (6)$$
$$u = \frac{k_0 \phi^2}{\mu L} \Delta p \qquad (7)$$

where u is the flow velocity, k is the permeability, ϕ is the porosity, Δp is the pressure change along each ridge segment at the specified depth, μ is the dynamic viscosity, and L is the length of each ridge segment. The value of k_0 we chose is 10^{-9} m^2, which is the lower value in the range given by Sparks and Parmentier (1991), and is also within the range used by Katz (2008). For μ, the dynamic viscosity, a value of 1 Pa-s was chosen, which is the median of the range of values given by Sparks and Parmentier (1991), and is the value chosen by Katz (2008). The porosity values we used varied depending on the depth of the melt generation region. At depths of 10 km and 50 km, values of $\phi = 0.04$ and, $\phi = 0.02$ are chosen respectively as given by Katz (2008).

The length of each ridge segment, L, is measured by applying the spherical law of cosines and solving for the great circle distance along the sphere between each of the coordinates bounding each ridge segment. The version of the spherical law of cosines used is as follows:

$$L = cos^{-1}(\sin(\phi_1)\sin(\phi_2) + \cos(\phi_1)\cos(\phi_2)\cos(\Delta\lambda))R_e \qquad (8)$$

where L is the great circle distance along each ridge segment, ϕ_1 and ϕ_2 are the latitudes of the first and second coordinates, $\Delta\lambda$ is the change in longitude between the two coordinates, and R_e is the average radius of the Earth. Again, the spherical approximation is negligible for these distances, with errors of <0.6% calculated when compared with the Vincenty equation (Geoscience Australia).

In addition to the flow velocity, the Rossby number and Coriolis parameter for each ridge segment flow is calculated to demonstrate the degree to which the Coriolis accelerations from the Earth's rotation dictate the flow characteristics of magmatic focusing under the ridge system. The Rossby number (9) and Coriolis parameter (10) are calculated as:

$$Ro = \frac{U}{Lf} \qquad (9)$$
$$f = 2\Omega \, \sin(\phi) \qquad (10)$$

where Ro is the dimensionless Rossby number, U is the characteristic velocity which in this model is taken as the u fluid velocity calculated by Darcy's law

in equation (7), L is the characteristic length of each ridge segment, which is calculated in equation (8), f is the Coriolis parameter, ϕ is the latitude, and Ω is the rotation of the Earth (7.29212×10^{-5} Rad/s).

RESULTS
Tectonic Fabric Results

Along the MAR from 0 to 30° N, all 15 transform offsets exhibit left lateral faulting. Of the transform faults, 72% of faults are within 5° of perfect E-W orientations. The tight clustering of transform azimuths indicates that the orthogonal fracture pattern seen across the ridge system is associated with transform faulting. In contrast, only 19% of the non-transform ridge segments were within 5° of perfect N-S orientation due to the presence of more non-transform offsets, especially in the northern region of the study area. Rose diagram plots of the non-transform ridge segment azimuths and transform segment azimuths are shown in Figure 5a and Figure 5b respectively.
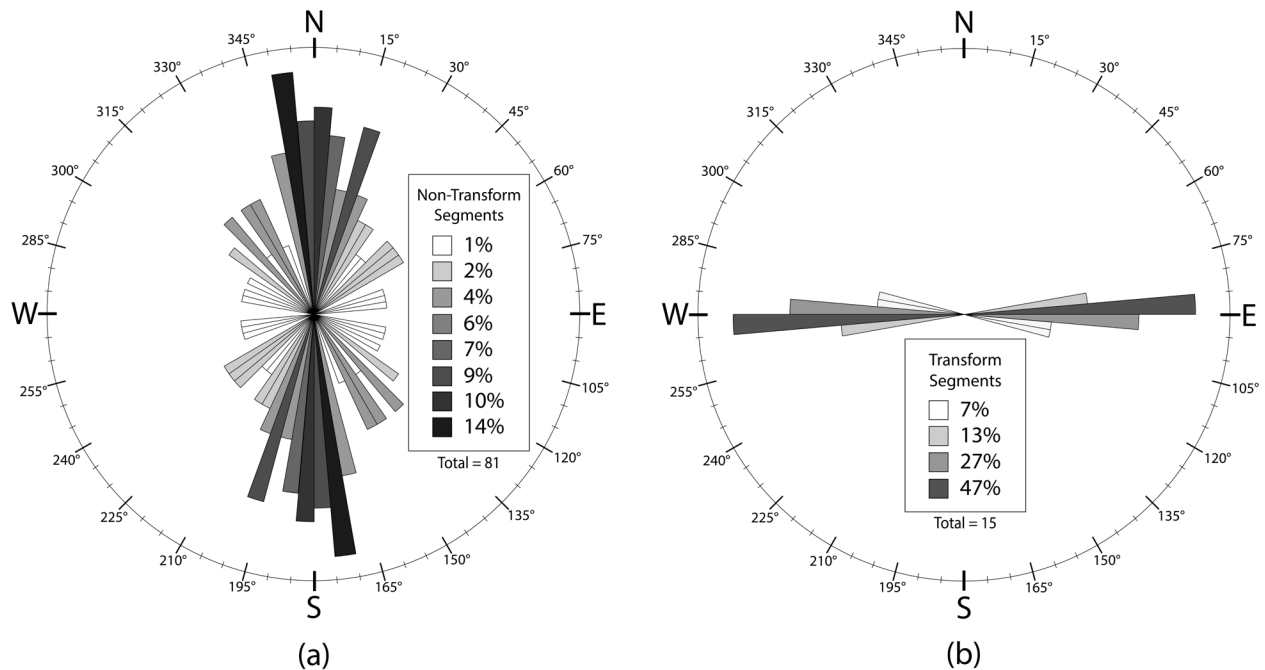
Figure 5. Rose diagrams showing azimuths of ridge segments (5a) and segments of transform faults along the ridge axis line (5b).

According to the rose diagram plots alone, the ridge system would appear to have a slight counterclockwise rotation on average, but this observation does not account for the rotation as a function of latitude. In Figure 6, rotation of transform faults and ridge segments is shown as a function of latitude. These plots indicate a correlation between stronger clockwise rotation and higher latitudes within the study area.

Depth and Load Results

Within each of the 423 average bathymetry buffers along the ridge axis, (excluding transform faults) load calculations at depth were most influenced by changes in bathymetric depth across the ridge due to the same crustal density assumptions throughout the study area. Differences in normal gravity across the range of latitudes had a very small impact on the lithostatic pressure due to the 0.1% variation in the acceleration from 9.780 m/s^2 at the equator and 9.793 m/s^2 at 30° N.
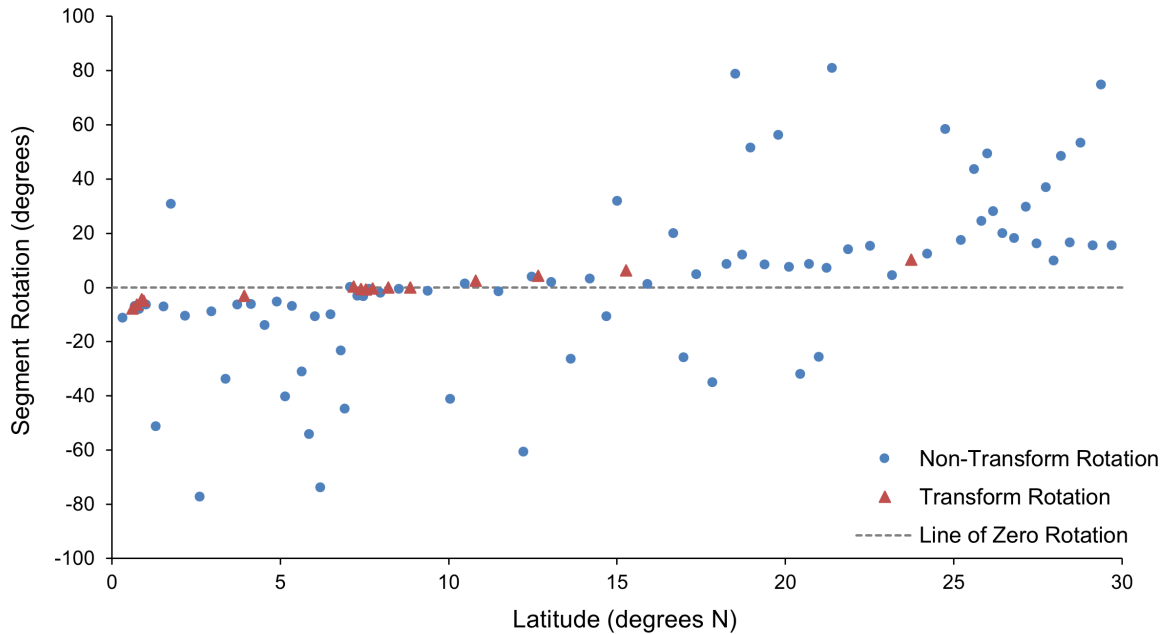
Figure 6. Representation of rotational character in segments relative to cardinal directions. Plot of non-transform (circle) and transform fault (triangle) segments by latitude. Non-transform segments are measured with respect to N-S and transform fault segments with respect to E-W.
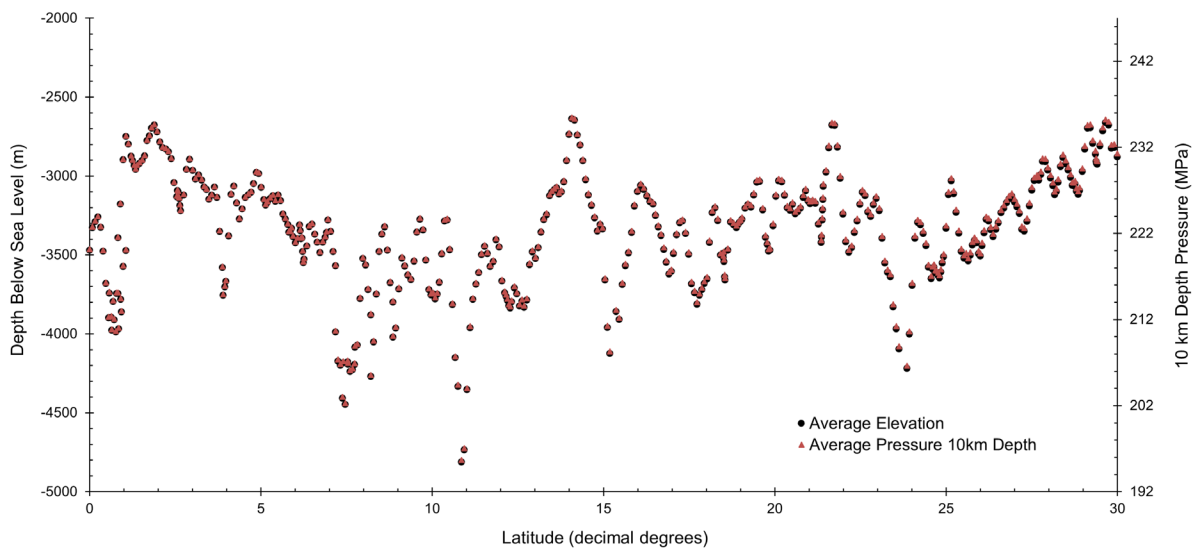
Figure 7. Average bathymetric relief and lithostatic pressure at a depth of 10 km plotted with respect to latitude for the study area.

Lithostatic pressure varied by an average of 1.46 MPa over each sampling interval across the ridge system at both the 10 and 50 km

depths. Between each of the 9 km spaced sampling points along the ridge at the 10 km depth, gravity was responsible for only a 450 Pa pressure difference on average, or 0.001% of the mean pressure variation between each sampling interval. Similarly, at the 50 km depth, variation in gravitational acceleration over the ridge was responsible for a 3100 Pa pressure difference between each sample point, or 0.007% of the average pressure variation between points at the 50 km depth.

In Figure 7 the lithostatic pressure at 10 km and the bathymetric depth are plotted showing the variation in bathymetric depth and the subsequent variations in the lithostatic loads across the MAR from 0 to 30° N. In Figure 8 the lithostatic pressures at 50 km and bathymetric depths are also plotted, but a slight deviation is shown in the two linear plots where small changes in gravitational acceleration amount to a divergence of the pressure from the bathymetric depth at distances further along the ridge.

Subaxial Flow Results

According to one-dimensional magma flows models using Darcy's law, at 10 and 50 km depths below the ridge axis, flow velocities within the melt generation region are at times comparable to upwelling velocities of 1-3 cm/yr cited in the literature (Sparks and Parmentier, 1991; Weatherley and Katz, 2010). The predicted flows related to axial variation in lithostatic pressure are indicative of pressure gradients significant enough to enable northward and southward flow directions along the ridge axis in areas of continuous magmatic focusing along ridge segments.

The predicted average flow magnitude across the ridge system is 0.8 cm/yr at a depth of 10 km, and 0.2 cm/yr at a depth of 50 km. Subaxial magma flows caused by lithostatic pressure changes across the ridge system are also predicted at the 10 and 50 km depths and are displayed in Figures 9 and 10.
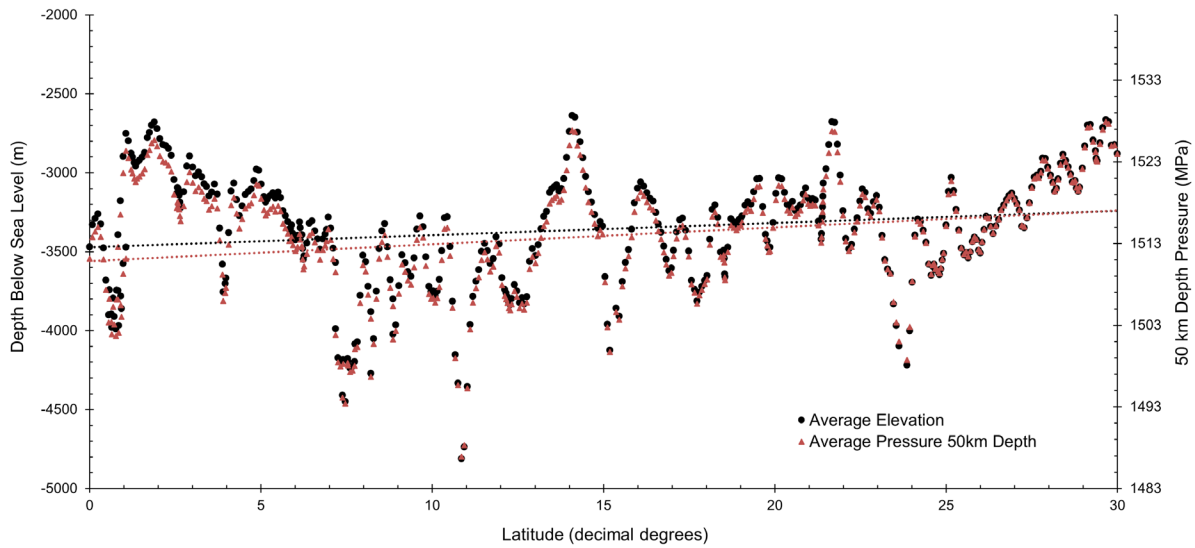
Figure 8. Average bathymetric relief and lithostatic pressure at a depth of 50 km plotted with respect to latitude for the study area.
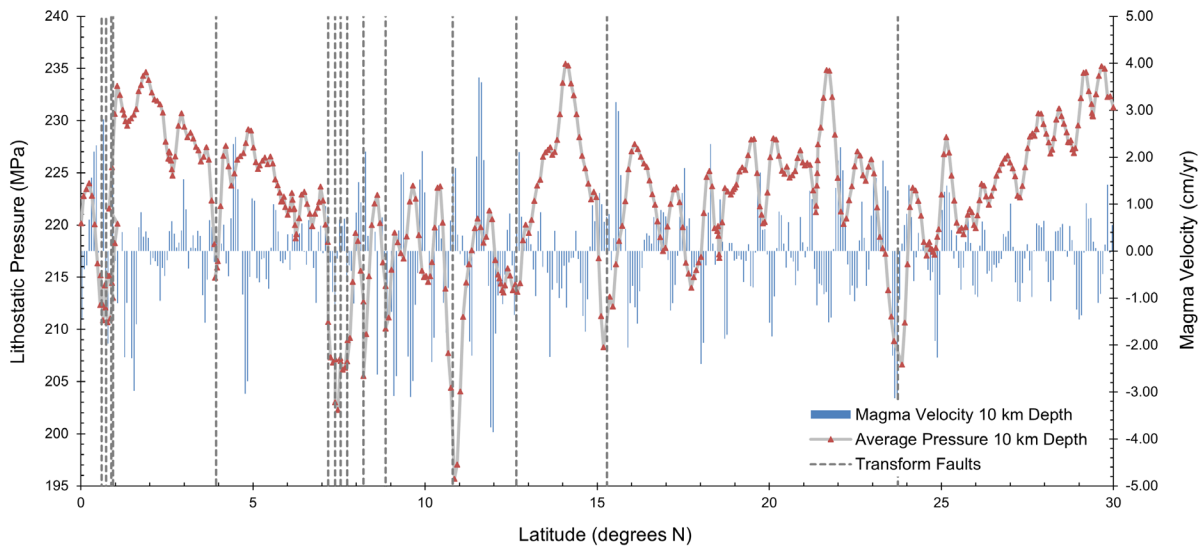
Figure 9. Magma velocity and average pressure at 10 km depth plotted with respect to latitude for the study area. Transform fault latitudes are also indicated.
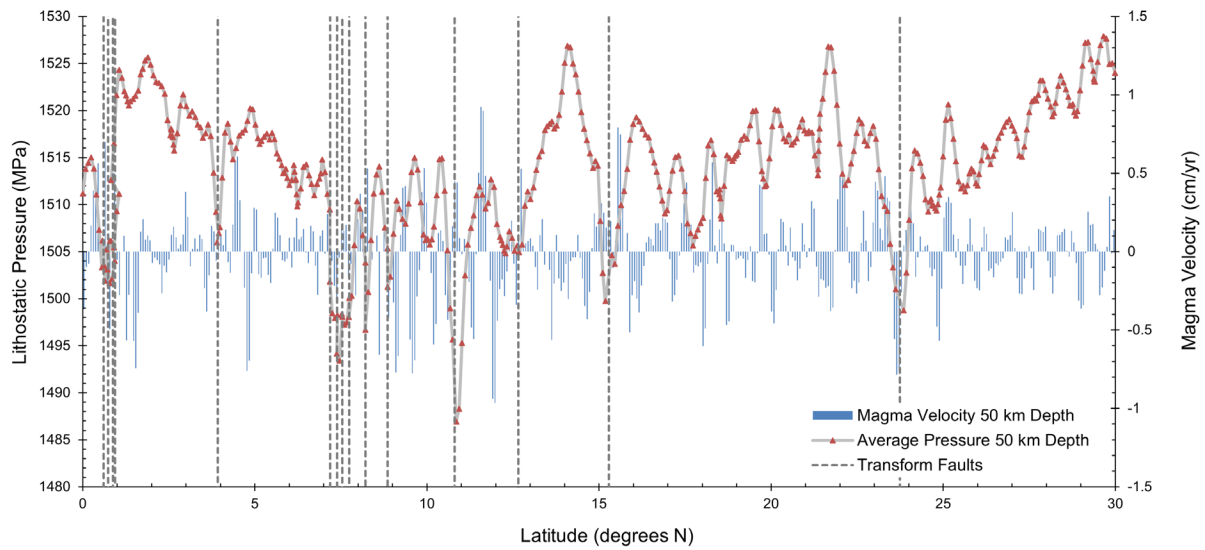
Figure 10. Magma velocity and average pressure at 50 km depth plotted with respect to latitude for the study area. Transform fault latitudes are also indicated.
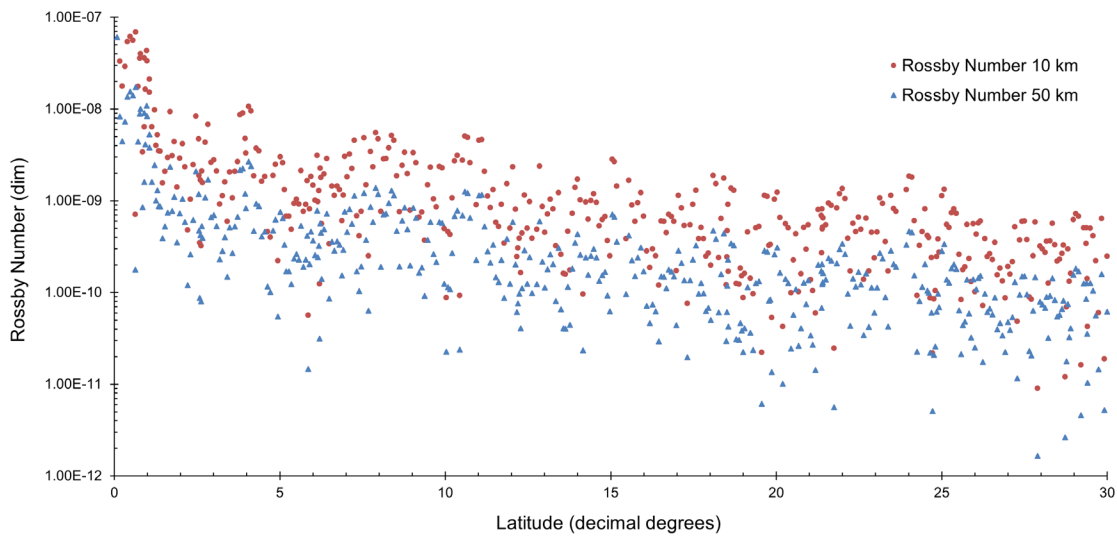
Figure 11. Rossby numbers plotted on a logarithmic axis for subaxial flow vectors along each ridge segment based on length, velocity, and Coriolis parameter with respect to latitude. Lower Rossby numbers indicate stronger Coriolis influence.

This analysis indicates significant flow velocities which are often comparable in magma transport speed to regional low porosity melt generation upwelling. Porosities within the melt generation and upwelling region below the solidus are expected to be approximately 4% and 2% at 10 and 50 km depths respectively (Katz, 2008). However, along the solidus boundary areas, a porosity value of up to 9% can be expected (Katz, 2008). Accounting for the high porosity at the boundary of the solidus, the model predicts an average subaxial flow magnitude of 4 cm/yr, which is 5 times higher than the expected average flow magnitude at a depth of 10 km within the melt upwelling region below the solidus.

The subaxial melt migration predicted in our model is expected to be impacted by the Coriolis parameter and thus produce rotational shearing. Rossby numbers calculated along the ridge axis show an expected drop from 0 to 30° along the MAR. This drop in the Rossby number indicates an increase in the significance of Coriolis influences on magma flow compared to the inertial forces on the magma. The Rossby number calculated for the subaxial flows for both the 10 and 50 km depths decreases from approximately 1×10^{-8} near the equator to 1×10^{-10} near 30° N. Rossby numbers along the ridge for both 10 and 50 km depths are plotted in Figure 11 on a logarithmic axis. Flows tend to have higher Rossby numbers at 10 km vs 50 km. This is expected due to predictions of lower velocities at lower depths below the ridge axis due to decreasing porosity.

DISCUSSION
Tectonic Fabric of the MAR

Two distinct regions of the tectonic fabric of the MAR within our study area can be recognized. Brittle deformation is evident in the lower latitude region (0 to 13° N) and ductile deformation is evident in the upper latitude region (23 to 30° N). Between the two regions, a transitional area exists within 13 to 23° N. The lower latitude region is characterized by frequent (13 of 15) transform faults and primarily orthogonal offsetting of ridge segments. In the upper latitude region, fewer transform faults are present, but shearing is accounted for by non-transform offsets in the ridge.

Transform faults across the study area exhibit left-lateral displacement and are generally accompanied by large fracture zones. An extremely deep (~7000 m) fracture zone known as the Romanche Gap straddles the Equator marking the southernmost boundary of the study area. Here, the Romanche Gap extends more than 900 km in length, crossing approximately 8° of longitude. Along the northernmost boundary of the study area, at around 30° N, the Atlantis Fracture Zone lies within the more ductile area of the upper latitude region of our study area and is not as deep or as pronounced as the Romanche Gap.

In the upper latitude region, the ridge curves in a northeasterly direction towards the triple-junction between the North American, African, and Eurasian plates. The shape of the ridge along this span of the MAR towards the triple junction is characterized by the same ductile deformation of the oceanic crust and is a continuation of the same pattern seen in the upper latitude region of the study area. By contrast, in the lower latitude region, the ridge axis is primarily oriented in a northwesterly direction towards the triple-junction between the Caribbean, North American and South American plates, exhibiting brittle deformation.

Subaxial Magma Flow

Since the flow model applied in this study is based on variations in lithostatic pressure, the flow velocities predicted are strongly dependent on changes in ocean depth. This relationship is most evident at a depth of 10 km, while at a depth of 50 km, a slight deviation from a linear relationship between pressure and bathymetry can be found. The deviation seen in the 50 km depth data is due to changes in gravitational acceleration with respect to latitude. This causes larger differences in the load because of the greater mass subject to gravitational acceleration, which in turn contributes to higher lithostatic load gradients at greater depths.

In our flow model, porosity also has a significant impact on the flow magnitude due to the assumptions made for Darcy's law. As shown in the results, the high-porosity layer at the boundary of the solidus predicts subaxial magma velocities five times

greater than flow velocities at the 10 km depth that experience the same pressure gradients determined by the bathymetry. One assumption made for this model is that at each depth, the porosity remains constant along the ridge within the melt generation regions at 10 and 50 km depths. However, the pressure gradients that are modeled in this study may also influence the porosity, which is not accounted for in this analysis. If a flow model could be applied that predicted the changes in porosity along the ridge caused by changes in load, the calculated flow magnitudes could be affected.

Potential Large Scale Flow Patterns

The potential exists for large flow patterns to be identified across first-order ridge segments where overall trends of increasing or decreasing depth yield consistent pressure gradients. However, the flow velocities and gradients within the study area are only calculated along 9 km intervals, since flows over longer distances would require the assumption that continuous magma flow is possible between all areas of high and low pressure. It is unclear that magma would be able to flow continuously across the ridge system with first and second-order discontinuities in the ridge acting as potential barriers to continuous subaxial flow. Given that it is likely that transform faults act as boundaries for continuous subaxial flow, these will be explored as the potential bounds on larger subaxial flow directions beneath the ridge system.

The first potential area of larger scale subaxial magma flow exists in the upper latitude region of the study area, between the Atlantis and Kane Fracture Zones. Along this large first-order ridge segment, ocean depth generally increases southward. The bathymetric analysis and respective load calculations support a pressure gradient that decreases from 30 to 24° N and could support the interpretation of overall subaxial flow to the south along this ridge segment.

The second area where larger scale subaxial magma flow could exist is below the two longest first-order ridge segments within the lower latitude region. The two ridge segments span 1 to 4° N and 4 to 7° N, and each exhibit decreasing pressure

with increasing latitude due to the increasing ocean depth across these two first-order ridge segments. Subaxial magma flows in this region could travel northward within the confines of the transform bounds of these two larger ridge segments. Large scale subaxial flow patterns such as these would yield the greatest opportunity for deflection by Coriolis.

Rotational Patterns in the MAR

Increasing clockwise rotation of ridge segments is seen across the ridge system moving northward. This is the expected pattern of rotation assuming the Coriolis parameter is correspondingly driving rotational motion clockwise in magma flows in the Northern Hemisphere. Even though in the lower latitude region from 0 to around 8° N, the rotation of orthogonal fracture patterns is rotated counterclockwise with respect to north, subsequent rotations moving northward continue to rotate clockwise with respect to the previous segment.

Here in the rotation data, an interesting pattern can be observed. 9 out of 11 transforms found from 0 to 10° N had counterclockwise-rotated azimuths with reference to a perfect E-

W orientation, while all four transforms located between 10 to 30° N exhibited clockwise-rotated azimuths. We hypothesize that between approximately 0 to 8° N, other factors and forces have acted on the transform faults in this area, which causes their azimuths to defer in a direction opposite to what we would expect to see due to the Coriolis parameter. Higher resolution bathymetry within the 7 to 10° N span would aid further insights into the potential causes for the pattern seen in transforms in this region. The fact that only 2 out of the 15 transform faults in our study area are located within the 15 to 30° N range supports our observation that the southern half of our study area exhibits a much higher rate of faulting and tectonic activity when compared to the northern half.

Coriolis as an Explanation of Rotation

Based on the Rossby numbers calculated for the upper latitude region of the study area, there is an increased potential for shearing forces derived from the Coriolis parameter when compared with lower latitudes. Rossby number analysis also indicates that the

Coriolis parameter exerts the smallest amount of influence in the equatorial region, and hence, minimal influence by rotational shear is seen. The equator is instead dominated by transform faulting and orthogonal fracturing.

The Coriolis parameter has also been established as a rotation-inducing factor. Coriolis-induced flows cause circulations on a global scale that have opposite effects between the Northern and Southern hemispheres. Due to the rotation of the Earth, fluids in the Northern Hemisphere undergo an apparent clockwise deflection, while fluids in the Southern Hemisphere undergo an apparent counterclockwise deflection. The effect of the Coriolis parameter can be seen in a plethora of phenomena, from wind patterns and ocean currents to (in our belief) magma flow. Taking all the factors influencing magma migration into consideration, and in conjunction with discussions in the literature, the Coriolis parameter may have some role to play in subaxial magma migration (Khutorskoi and Teveleva, 2019).

Furthermore, the effect of the Coriolis force can be seen on transform faults as well. This is demonstrated in Figure 6, as explained previously, which shows the increasing clockwise rotation of transform fault azimuths that could be the result of the influence of Coriolis. This established pattern shows continued clockwise rotation moving northward along ridge segments and transforms in the study area.

Flows induced by Coriolis may also be responsible for the left-lateral displacement (caused by shear forces) apparent in all the transform azimuths we examined. Ridge segments also take on an increasing clockwise rotation with respect to a N-S orientation throughout the study area. Clockwise rotation within magma flows in the Northern Hemisphere would be caused by the Coriolis parameter. We would also expect that the influence due to Coriolis would be greater in the upper latitudes compared with the lower latitudes as evidenced by the decreasing Rossby number with increasing latitude.

In the upper latitude region of the study area, as explained before, there is a potential for large scale subaxial magma flows not impeded by transform faults. As a result of Coriolis shearing, continuous subaxial flow may contribute to the large-scale

morphology of the ridge with flows not sharply cut off by transform faults. As is evident in the bathymetry of this region, the ridge segments are more angled and shear forces exhibited on this zone do not result in a high frequency of transform faulting as seen in the lower latitude region.

Other Explanations of Rotational Patterns

With patterns in the fabric of the MAR recognized, flow potential established, and Coriolis considered, we proceed by evaluating other factors that could influence the MAR's tectonics over time. As with all active mid-ocean ridge systems, primary tensional stresses produce a divergent margin. Divergent plate motion alone is expected to produce primary tension fractures perpendicular to the direction of tensional stress, as well as secondary fractures related to the associated shearing at approximately 60° to the direction of tension. The first and primary direction of tensional stress currently acting on the MAR system is attributed to the relative divergence between the South American and African plates. Divergence to produce orientation of

the ridge segments in the lower latitudes as observed and without rotation would require a divergence direction of ENE-WSW. When there are two sets of tension fractures at 90° to each other, a secondary direction of tensional stress can be inferred which is perpendicular to the first. To produce the orthogonal fractures serving as transform faults, a secondary tensional stress field would need to be oriented at NNW-SSE. This secondary stress field could be associated with mantle upwelling or equatorial bulge.

In the upper region of the study area in the north, the relationship changes as divergence occurs between the North American and African plates. Azimuthal orientations of the ridge and non-transform segments without rotation would suggest primary plate divergence in this section of the rift with an orientation of WNW for the North American Plate, and ESE for the African Plate. There are fewer orthogonal offsets in this northern area due to transforms or fracture zones. However, if there was a perpendicular tensional stress field to produce these fractures and faults, it would need to be oriented NNE-SSW.

The orientation of the stress field during initial fracturing may have differed from the current observed stress orientation. In the oceanic crust long the MAR, there is evidence of asymmetry and variable spreading rates (Müller et al., 2008). These differences are not enough to account for a shift in fault orientation of fracture zones that is indicated by the clockwise rotation exhibited within the northern part of our study area. However, it is worthwhile to consider the geometry during the opening of the Atlantic Ocean that could show inherited fracture orientations that should be demonstrated in changes in spreading rates as the oceanic crust developed. With the opening of the Atlantic in the Northern Hemisphere first followed by the Southern Hemisphere, divergence could be oriented to the WNW-ESE, change to E-W, and then shift to ENE-WSW. To accommodate such a shift, the African Plate would need to exhibit large-scale counterclockwise rotation, which is unlikely. Conversely, if the African Plate was stationary, there would need to be a relationship between the North American (WNW movement) and South American (WSW movement) plates which would result in rifting on the western margins. This relationship is not evident in the current tectonics.

Relative spreading rates provide a planar perspective for understanding divergence. However, it is important to consider the global platform of the spherical surface as represented by the positioning of Euler poles. Thinking of Euler poles as hinges in plate rotation on a spheroid surface is beneficial to discussions of rotational phenomena. According to Moores and Twiss (2014), the Euler pole represents the intersection of the axial rotation of two plates relative to one another with the surface of the Earth. Angular velocities of plate divergence would increase with distance, maximizing at 90° from the Euler pole. The Euler pole would need to shift from the southern Atlantic to the northern Atlantic to explain the observed changes in rotation if divergence alone accounts for the orientation of ridge and transform segments. If this were the case, digital models of ocean spreading would show distinct changes in axial divergence rates with time.

Another tectonic factor at work adjacent to the study area is the subduction of the North American Plate

with respect to the Caribbean Plate to produce the Puerto-Rican Trench and the Lesser Antilles volcanic island arc. This specific configuration with subduction to the west, is likely to exert additional tensional stress on the west side of the MAR system in the latitudes ranging from 13 to 20° N producing variable rates and increased asymmetry. This study indicates that a transition area occurs along the MAR from 13 to 23° N where the character of the fracture orientation changes. It's likely that the influence of subduction contributes to the variations seen within this transition between the lower and upper regions of our study area.

Errors in Bathymetry Data

For the areas of the GEBCO bathymetry data that were derived from satellite measurements, data was interpolated between single bathymetric soundings and satellite altimetry data along with any surrounding sonar derived bathymetry. The base source for the satellite data included in the GEBCO 2020 Grid is the SRTM15+V2.0 dataset produced by Tozer and others, 2019. According to the analysis of the base satellite altimetry data, there is an estimated error of ±150 m for the deep ocean (Tozer et al., 2019).

In our own analysis of the data, sections of the satellite derived bathymetry were found that have a depth error of more than 500 m near isolated features such as the Saint Peter and Saint Paul Archipelago (0°55'00" N, 29°20'44'' W). This feature is located directly along the MAR ridge axis of divergence within the study area. This archipelago has a reported depth of approximately 800 m below sea level in the GEBCO 2020 Grid. However, there should be land a few meters above sea level on each of the islands. The cause of this deviation is likely the lower crustal density in this region due to the fact that it formed via uplift instead of by volcanism (Motoki et al., 2014). This lower density causes a free-air gravity anomaly that is lower than would be expected for topography above sea level. Additionally, there appears to be a lack of sufficient bathymetric soundings or multi-beam sonar data available in the vicinity of the archipelago to sufficiently constrain the interpolation with satellite data for the region.

Similarly, our analysis found that topographic data for the Rocket

Seamount (15°50'50" N, 36°9'28" W) reports an elevation of up to 24 m above sea level for the feature, while the top of the seamount should appear at a depth of 630 m below sea level (Il'in, 1998). In this case, we suspect that increased crustal density and a lack of nearby bathymetric soundings or multi-beam sonar scans in the area led to this error. However, in this case, the Rocket Seamount is not close enough to the ridge to affect the calculations and modeling performed in the present study. Regardless, it still acts as an indication of the potential deviation from true topography that exists within the satellite derived data.

However, despite these identified errors with the satellite derived bathymetry contained in the GEBCO 2020 dataset, the erroneous bathymetry is unlikely to significantly affect the results of the analysis since sampling for the present analysis is done over large geographic areas. The ridge segment azimuth sampling in our study area accounts for changes over large segments of the MAR, and loads are calculated with circular buffers of 20 km in radius.

CONCLUSIONS

This study provides strong evidence supporting subaxial magma flows driven by lithostatic pressure gradients at depths of 10 and 50 km within the melt prism. The subaxial flow velocities predicted by our model suggest magnitudes on the same scale as modeled upwelling rates beneath the ridge. We conclude that axial topographic variation as seen at the slow spreading ridge of the MAR system is an excluded variable within current models. Future research may incorporate topographic variation in conjunction with other flow parameters to accurately model magma migration below mid-ocean ridges. More research is needed in areas of the MAR with low-resolution bathymetry such as within the 7 to 10° N range. To accurately model large-scale phenomena for subaxial magma migration, geophysical studies are needed to provide constraints on porosity, compositional changes in the ocean crust and upper mantle, and thermal gradients. Given the calculated magma velocities in the study area, we expect flow patterns to be influenced by Coriolis as an explanation of observed rotation and shearing. In addition to

Coriolis, there may be other explanations of rotational deflection exhibited in the fracture and fault morphology such as mantle plumes, or decoupled lithosphere-asthenosphere motion.

DATA SOURCES

GEBCO Compilation Group (2020) GEBCO 2020 Grid (doi:10.5285/a29c5465-b138-234d-e053-6c86abc040b9)

Tozer, B, Sandwell, D. T., Smith, W. H. F., Olson, C., Beale, J. R., and Wessel, P. (2019). Global bathymetry and topography at 15 arc sec: SRTM15+, distributed by OpenTopography. https://doi.org/10.5069/G92R3PT9

Vincenty Geodetic Calculator. Commonwealth of Australia (Geoscience Australia) 2021

REFERENCES

Asimow, P.D., and Langmuir, C.H., 2003. The Importance of Water to Oceanic Mantle Melting Regimes. *Nature*, vol. 421, no. 6925, pp. 815–820., doi:10.1038/nature01429.

Auzende, J., Cannat, M., Gente, P., Henriet, J., Juteau, T., Karson, J., Lagabrielle, Y., Mével, C., and Tivey, M., 1994. Observation of Sections of Oceanic Crust and Mantle Cropping out on the Southern Wall of Kane FZ (N. Atlantic). *Terra Nova*, vol. 6, no. 2, pp. 143–148., doi:10.1111/j.1365-3121.1994.tb00647.x.

Briais, A., Sloan, H., Parson, L.M., and Murton, B.J., 2000. Accretionary Processes in the Axial Valley of the Mid-Atlantic Ridge 27° N-30° N From TOBI Side-Scan Sonar Images. *Marine Geophysical Researches,* vol. 21, pp. 87–119.

Brown, J.W., and White, R.S., 1994. Variation with Spreading Rate of Oceanic Crustal Thickness and Geochemistry. *Earth and Planetary Science Letters*, vol. 121, no. 3-4, pp. 435–449., doi:10.1016/0012-821x(94)90082-5.

Canales, J.P., Tucholke, B.E., and Collins, J.A., 2004. Seismic Reflection Imaging of an Oceanic Detachment Fault: Atlantis Megamullion (Mid-Atlantic Ridge, 30°10'N). *Earth and Planetary Science Letters*, vol. 222, no. 2, pp. 543–560., doi:10.1016/j.epsl.2004.02.023.

Carbotte, S.M., and Macdonald, K.C., 1994. Comparison of seafloor tectonic fabric at intermediate, fast, and super fast spreading ridges: Influence of spreading rate, plate motions, and ridge segmentation on fault patterns. *Journal of Geophysical Research: Solid Earth*, 99(B7), 13609-13631.

Cormier, M., Detrick, R.S., and Purdy, G.M., 1984. Anomalously Thin Crust in Oceanic Fracture Zones: New Seismic Constraints from the Kane Fracture Zone. *Journal of Geophysical Research: Solid Earth*, vol. 89, no.

B12, pp. 10249–10266., doi:10.1029/jb089ib12p10249.

Dasgupta, R., and Hirschmann, M.M., 2010. The Deep Carbon Cycle and Melting in Earth's Interior. *Earth and Planetary Science Letters*, vol. 298, no. 1-2, pp. 1–13., doi:10.1016/j.epsl.2010.06.039.

Il'in, A.V., 1998. On the Origin and Evolution of the Atlantis, Cruiser, Meteor, Rocket and Krylov Seamounts in the Atlantic Ocean. *Oceanology*, vol. 40, no. 6, pp. 856–867.

Katz, R.F., 2008. Magma Dynamics with the Enthalpy Method: Benchmark Solutions and Magmatic Focusing at Mid-Ocean Ridges. *Journal of Petrology*, vol. 49, no. 12, pp. 2099–2121., doi:10.1093/petrology/egn058.

Kelley, K.A., 2014. Inside Earth Runs Hot and Cold. *Science*, vol. 344, no. 6179, pp. 51–52., doi:10.1126/science.1252089.

Khutorskoi, M.D., and Teveleva., E.A., 2019. Nature of Heat Flow Asymmetry on the Mid-Oceanic Ridges of the World Ocean. *Oceanology*, vol. 60, no.

1, pp. 108–119., doi:10.1134/s0001437020010142.

Lin, J., and Parmentier, E.M., 1989. Mechanisms of Lithospheric Extension at Mid-Ocean Ridges. *Geophysical Journal International*, vol. 96, no. 1, pp. 1–22., doi:10.1111/j.1365-246x.1989.tb05246.x.

Liu, L., Lu, J., Tao, C., and Liao, S., 2021. Prospectivity Mapping for Magmatic-Related Seafloor Massive Sulfide on the Mid-Atlantic Ridge Applying Weights-of-Evidence Method Based on GIS. *Minerals*, vol. 11, no. 1, pp. 1-23., doi:10.3390/min11010083.

Long, X., Geldmacher, J., Hoernle, K., Hauff, F., Wartho, J., Garbe-Schöenberg, D., and Grevemeyer, I., 2019. Age and Origin of Researcher Ridge and an Explanation for the 14°N Anomaly on the Mid-Atlantic Ridge by Plume-Ridge Interaction. *Lithos*, vol. 326-327, pp. 540–555., doi:10.1016/j.lithos.2019.01.005.

Macdonald, K.C., Scheirer, D.S., and Carbotte, S.M., 1991. Mid-Ocean Ridges: Discontinuities, Segments and Giant Cracks. *Science*, vol. 253, no. 5023, pp. 986–994., doi:10.1126/science.253.5023.986.

Macdonald, K.C., and Fox, P.J., 1990. The Mid-Ocean Ridge. Scientific American, vol. 262, no. 6, pp. 72–81.

Marcia, M., Sichel, S., Briais, A., Brunelli, D., Ligi, M., Ferreira, N., Campos, T., Mougel, B., Brehme, I., Hemond, C., Motoki, A., Moura, D., Scalabrin, C., Pessanha, I., Alves, E., Ayres, A., and Oliveira P., 2016. Extreme Mantle Uplift and Exhumation along a Transpressive Transform Fault. *Nature Geoscience*, vol. 9, no. 8, pp. 619–623., doi:10.1038/ngeo2759.

Mallows, C., and Searle, R.C., 2012. A Geophysical Study of Oceanic Core Complexes and Surrounding Terrain, Mid-Atlantic Ridge 13°N-14°N. *Geochemistry, Geophysics, Geosystems*, vol. 13, no. 6, pp. 1-27., doi:10.1029/2012gc004075.

Mohriak, W., 2020. Genesis and Evolution of the South Atlantic Volcanic Islands Offshore Brazil. *Geo-Marine Letters*, vol. 40, no. 1, pp. 1–

33., doi:10.1007/s00367-019-00631-w.

Moores, E.M., and Twiss, R.J., 2014. *Tectonics*. Waveland Press, IL 415 p.

Motoki, K.F., Motoki, A., and Sichel, S.E., 2014. Gravimetric Structure for the Abyssal Mantle Massif of Saint Peter and Saint Paul Peridotite Ridge, Equatorial Atlantic Ocean, and Its Relation to Active Uplift. Anais Da Academia *Brasileira De Ciências*, vol. 86, no. 2, pp. 571–588., doi:10.1590/0001-37652014117712.

Müller, R.D., Roest, W.R., Royer, J.Y., Gahagan, L.M., and Sclater, J.G., 1997. Digital Isochrons of the World's Ocean Floor. *Journal of Geophysical Research: Solid Earth*, vol. 102, no. B2, pp. 3211–3214., doi:10.1029/96jb01781.

Niu, Y., and Batiza, R., 1991. In Situ Densities of Morb Melts and Residual Mantle: Implications for Buoyancy Forces beneath Mid-Ocean Ridges. *The University of Chicago Press*, vol. 99, no. 5, pp. 767-775.

Office of Geomatics, 2014. National Geospatial-Intelligence Agency (NGA) Standardization Document: Department of Defense World Geodetic System 1984 – It's Definition and Relationships with Local Geodetic Systems. *Office of Geomatics National Geospatial-Intelligence Agency*, Version 1.0.0.

Plank, T., and Langmuir, C.H., 1992. Effects of the Melting Regime on the Composition of the Oceanic Crust. *Journal of Geophysical Research*, vol. 97, no. B13, p. 19749., doi:10.1029/92jb01769.

Roest, W.R., and Collette, B.J., 1986. The Fifteen Twenty Fracture Zone and the North American–South American Plate Boundary. *Journal of the Geological Society*, vol. 143, no. 5, pp. 833–843., doi:10.1144/gsjgs.143.5.0833.

Simon, N.S.C., Neumann, E., Bonadiman, C., Coltorti, M., Delpech, G., Gregoiré, M., and Widom, E., 2008. Ultra-refractory Domains in the Oceanic Mantle Lithosphere Sampled as Mantle Xenoliths at Ocean Islands. *Journal of Petrology*, vol. 49, no. 6,

pp. 1223-1251., doi:10.1093/petrology/egn023.

Sparks, D.W., and Parmentier, E.M., 1991. Melt Extraction from the Mantle beneath Spreading Centers. *Earth and Planetary Science Letters*, vol. 105, no. 4, pp. 368–377., doi:10.1016/0012-821x(91)90178-k.

Spathopoulos, F., and Jones, E.J.W., 1993. Seismic Evidence for Anomalous Crustal Structure beneath Mesozoic Fracture Zones in the Gambia Basin, Eastern Equatorial Atlantic. *Tectonophysics*, vol. 225, no. 3, pp. 205–217., doi:10.1016/0040-1951(93)90280-w.

Tozer, B., Sandwell, D.T., Smith, W.H.F., Olson, C., Beale, J.R., and Wessel, P., 2019. Global Bathymetry and Topography at 15 Arc Sec: SRTM15+. *Earth and Space Science*, pp. 1847-1864., https://doi.org/10.1029/2019EA000658

Weatherley, S.M., and Katz, R.F., 2010. Plate-Driven Mantle Dynamics and Global Patterns of Mid-Ocean Ridge Bathymetry. *Geochemistry, Geophysics, Geosystems*, vol. 11, no. 10, pp. 1-15., doi:10.1029/2010GC003192.